PartGS: Learning Part-aware 3D Representations by Fusing 2D Gaussians and Superquadrics

Zhirui Gao Renjiao Yi Yuhang Huang Wei Chen Chenyang Zhu Kai Xu

National University of Defense Technology

Abstract

*Low-level 3D representations, such as point clouds, meshes, NeRFs, and 3D Gaussians, are commonly used to represent 3D objects or scenes. However, human perception typically understands 3D objects at a higher level as a composition of parts or structures rather than points or voxels. Representing 3D objects or scenes as semantic parts can benefit further understanding and applications. In this paper, we introduce **PartGS**, **part**-aware 3D reconstruction by a hybrid representation of 2D **G**aussians and **S**uperquadrics, which parses objects or scenes into semantic parts, digging 3D structural clues from multi-view image inputs. Accurate structured geometry reconstruction and high-quality rendering are achieved at the same time. Our method simultaneously optimizes superquadric meshes and Gaussians by coupling their parameters within our hybrid representation. On one hand, this hybrid representation inherits the advantage of superquadrics to represent different shape primitives, supporting flexible part decomposition of scenes. On the other hand, 2D Gaussians capture complex texture and geometry details, ensuring high-quality appearance and geometry reconstruction. Our method is fully unsupervised and outperforms existing state-of-the-art approaches in extensive experiments on DTU, ShapeNet, and real-life datasets.*

1. Introduction

3D reconstruction from multi-view images is a long-studying problem in 3D vision and computer graphics. Most reconstructed scenes are in low-level representations such as point clouds, voxels, or meshes, which differ from human perception. Humans understand 3D scenes as different semantic parts [26]. For instance, when observing a scene, we mentally construct high-level structural information, such as scene graphs, rather than point clouds or detailed geometry. Thus, we propose to learn part-aware scene reconstruction to decompose scenes into different individual semantic shapes or parts, facilitating tasks including physical simulation, manipulation/editing, 3D content generation, etc.

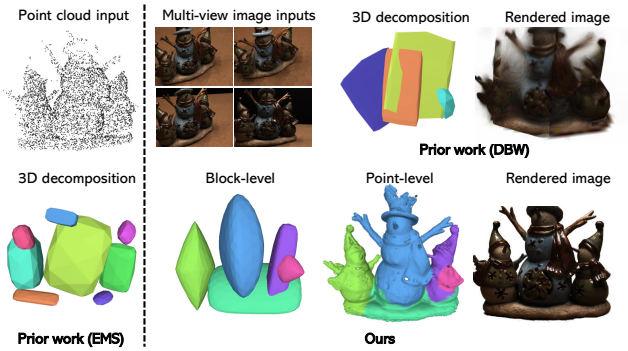

Figure 1. We propose a pipeline to reconstruct the scene in a part-aware manner. Prior works [22, 27] model the scene using primitives, while the proposed method can further model precise geometry details and textures. Here, EMS [22] takes point cloud inputs and reconstructs non-textured primitives.

There are prior methods [2, 20, 22, 23, 28, 36, 38, 42, 44, 48, 51] working on this topic, while they mainly learn the goal with 3D supervisions and cannot preserve accurate geometries, which leaves inconvenience to apply in realistic scenarios. While NeRF [25] has demonstrated great potential in reconstructing textured 3D scenes from multi-view images, some approaches [37, 49] try to learn part-aware objects via NeRFs. In particular, Part-NeRF [37] represents an object as multiple neural radiance fields. However, the complex composition of multiple implicit fields increases learning difficulty, resulting in subpar rendering quality and insufficient semantic decomposition. Another state-of-the-art approach DBW [27] decomposes scenes into blocks represented by superquadric primitives [2], optimizing their parameters and UV texture maps by minimizing rendering loss. Although DBW effectively decomposes 3D scenes into reasonable parts, learning accurate part-aware geometry and appearance still proves challenging as shown in Fig. 1.

To tackle the problem, we propose PartGS, a part-aware hybrid representation that integrates 2D Gaussians [16] and superquadrics [2] to reconstruct scenes that are both well-textured and geometrically accurate. There are previous approaches [13, 15, 39] combining mesh reconstruction and

Gaussian splatting, where they first reconstruct the mesh and then attach Gaussians to it. Their purpose is to get both representations, while our goal is to get part segmentation and reconstruction at the same time. Our method directly learns superquadric mesh and Gaussians simultaneously by coupling parameters between them while constraining each part to be represented as a single superquadric. The rendering capability of coupled Gaussians drives the optimization of hybrid representation, enabling the use of their convexity to assist in the decomposition of shapes. The unsupervised training of part-aware reconstruction is built upon the assumption that each functional part of most objects should be a basic shape and can be represented by a superquadric. On the other hand, Gaussian splatting, renowned for its superior rendering capabilities and efficient training[11, 18, 24], is incorporated to capture intricate texture details, speeding up reconstruction and improving rendering quality significantly. In the hybrid representation, 2D Gaussians are attached to the surface of superquadrics, with their pose and shape parameters coupled to the corresponding superquadric mesh. Compared to the vanilla Gaussian [18] that fills up the whole occupancy with individual-parameter 3D Gaussians, our method is more compact and efficient. The optimized parameters include global ones controlling the overall shape, pose, and opacity of hybrid blocks, and local parameters for spherical harmonic coefficients of the Gaussians.

During training, the parameters are optimized by rendering loss without additional supervision. We observe that image rendering loss tends to settle into local minima during the optimization of superquadrics. To address this, we design several regularizers to enforce global consistency between the 3D representation and the input 2D information. This allows us to segment parts in a fully unsupervised manner, achieving block-level reconstruction. At last, to model the accurate geometry, we conduct a point-level refinement, freeing 2D Gaussians to get out of the surface, thereby improving the modeling of irregular shapes. Contributions are summarized as follows:

- A novel hybrid representation is introduced to learn part-aware textured 3D scenes. The hybrid representation combines the benefits of both superquadrics and Gaussian splitting, enabling accurate part reconstruction and efficient high-quality rendering.
- An end-to-end unsupervised pipeline is proposed for block-level and point-level part-aware reconstruction, with superquadric meshes and 2D Gaussians optimized simultaneously by novel regularizers.
- Extensive experiments on public datasets demonstrate the superiority of the proposed method in part-aware reconstruction, enabling applications of part augmentation and physical interactions.

2. Related Works

2.1. Primitive-based 3D Representation

Learning structured shape representations aims to decompose objects or scenes into semantically coherent geometric primitives, providing a crucial pathway to shape understanding and generation [9, 14, 35, 41, 43, 50]. The earliest classical approaches, dating back to the last century, such as Blocks World [32] and Generalized Cylinders [3] emphasize compactness as the central goal. A substantial amount of prior work has focused on processing 3D data inputs, such as point clouds, meshes, and voxel grids. These methods decompose the 3D data into various types of primitive ensembles, including cuboids [31, 38], superquadrics [22, 29, 30, 44], and convex shapes [8, 10]. MonteBoxFinder [31], uses a RANSAC-based [12] with cuboids to represent point clouds, combined with Monte Carlo Tree Search for optimal selection. Alternatively, EMS [22] employs superquadrics to represent geometric primitives and proposes a probability-based approach to recover primitives. These methods rely on perfect 3D data, which is rarely available due to incompleteness or noise.

Few studies [1, 27, 37, 49] have attempted to create structure-aware 3D representations directly from images. PartNeRF [37] uses ellipses with neural radiance fields, but this spatial-based decomposition limits its ability to capture meaningful structural information. ISCO [1] and DBW [27] use 3D superquadrics for shape decomposition, which enables more meaningful structural separation. However, their simple shape parameters struggle to capture complex geometries, leading to poor geometry and appearance reconstruction. DPA-Net [49] has advanced 3D shape abstraction from sparse views but generates redundant parts and struggles with realistic texture rendering. Our approach introduces a hybrid representation that learns part-aware 3D scenes while ensuring accurate structural reconstruction and efficient, high-quality rendering.

2.2. Mesh-based Gaussian Splatting

Gaussian splatting(GS) [18] has been rapidly adopted in multiple fields due to its remarkable rendering capability. Several studies [7, 13, 15, 39] attempt to align Gaussians with mesh surfaces for easier editing and animation. Among them, SuGaR [15] uses flat 3D Gaussians to enforce the alignment with the scene surface during optimization, minimizing the difference between the signed distance functions (SDF) of the desired Gaussians and actual Gaussians. GaMeS [39] introduces a hybrid representation of Gaussians and mesh, where Gaussians are attached to triangular facets of the mesh. Similarly, Gao *et al*. [13] proposes a mesh-based GS to achieve large-scale deformation effects on objects. Recently, 2DGS [16] proposes 2D Gaussians for surface modeling and significantly enhances the geomet-

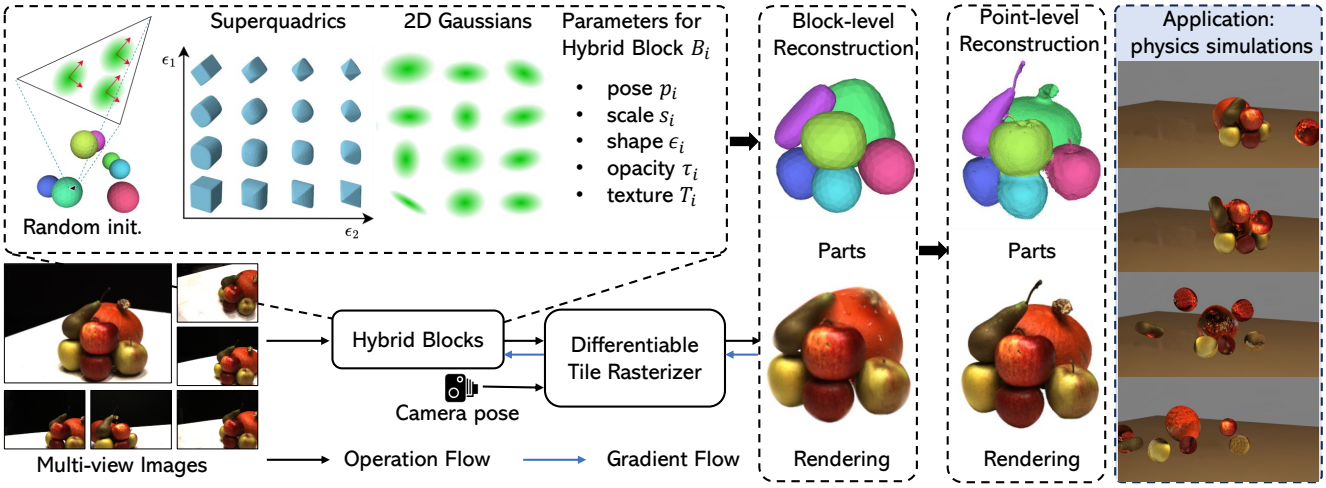

Figure 2. **Overview of PartGS.** PartGS takes multi-view images as input to learn a parametric hybrid representation of superquadrics and 2D Gaussians. The representation initializes from random superquadrics and is gradually optimized during training to get a block-level reconstruction. Then, we free the constraints of Gaussians to model detailed geometry to get a point-level reconstruction. The last column demonstrates one application of PartGS: physics simulations, where one part is picked up from the scene and thrown forward. Please refer to the supplementary materials for more video demos.

ric quality. Inspired by them, we propose a representation that combines 2D Gaussians with superquadrics. A key distinction between our method and previous mesh-based GS approaches is that these methods require first reconstructing the scene's mesh and then binding Gaussians to the mesh surface, which results in a non-continuous mesh. In contrast, our method directly optimizes the mesh through a rendering loss, enabling part-aware mesh reconstruction.

3. Method

Given a set of calibrated multi-view images, our goal is to learn part-aware 3D geometry and appearance. A part-aware reconstruction is often represented as a composition of multiple basic shapes (geometric primitives). We propose a primitive-based hybrid representation in Sec. 3.1. In Sec. 3.2, we demonstrate how this hybrid representation is optimized to fit primitives as parts (block-level). In order to further detail the geometry of each part, the parameters of Gaussians are further refined to get a point-level reconstruction.

3.1. Hybrid Representation

As shown in Fig. 2, the proposed hybrid representation combines superquadrics with 2D Gaussians in a compact form. To leverage the strengths of both, we attach Gaussians to the surface of superquadric meshes. This representation retains the superquadric's ability to effectively parse a 3D scene into distinct parts. Meanwhile, spherical harmonics of Gaussians enable complex texture rendering via Gaussian splatting, addressing the texture learning limitations of previous work [22, 27, 31, 48]. Sharing pose parameters between superquadrics and 2D Gaussians further enhances the representation's efficiency.

The proposed hybrid model is parametric, controlled by both primitive and Gaussian parameters, which are optimized simultaneously. Considering a 3D scene $\mathcal{S}$, we parse it into multiple superquadrics, i.e. blocks. Each block is denoted by the hybrid representation: $\mathcal{S} = \mathcal{B}_1 \cup ...\mathcal{B}_i... \cup \mathcal{B}_M$. Here, $\mathcal{B}_i$ is the i-th hybrid block, and M is the total number of blocks. The hybrid blocks are defined using manually designed parameters that control pose, opacity, scale, shape, and texture. These parameters are optimized via differentiable rendering to parse the target scene.

Shape and Scale Parameters. For each hybrid block $\mathcal{B}_i$, its geometry is controlled by superquadric parameters [2]. More concretely, there are two shape parameters ϵ_1, ϵ_2 that define the superquadric mesh, along with three scale parameters s_1, s_2, s_3, which scale the 3D axes. Similar to the positioning of vertexes in an icosphere, the 3D position of a superquadric vertex can be obtained by:

$$\mathbf{v} = [s_1 \cos^{\epsilon_1}(\theta) \cos^{\epsilon_2}(\varphi); s_2 \sin^{\epsilon_1}(\theta); s_3 \cos^{\epsilon_1}(\theta) \sin^{\epsilon_2}(\varphi)], \quad (1)$$

where θ and φ represent the azimuth and elevation defined in the spherical coordinate, respectively. The shape and scale parameters are optimized during training, thus controlling the block deformation to learn part-aware geometry.

Pose Parameters. The pose of the i-th hybrid block is defined by its rotation $\mathbf{R}_i$ and translation $\mathbf{t}_i$. The vertex position from Eq. 1 is transformed from the local coordinate to world space as: $\hat{\mathbf{v}}_i^j = \mathbf{R}_i \mathbf{v}_i^j + \mathbf{t}_i$, where j indexes the vertices. In prior methods such as SuGaR [15] and GaMeS [39], Gaussians are placed on the reconstructed mesh, and they have individual poses and shapes for better appearance modeling. Differently, in our method, the role of Gaussians is to

construct a differentiable rendering that bridges images and superquadrics. To achieve this, we couple the parameters of Gaussians with superquadrics.

Given a posed superquadric, centers of Gaussians are determined by uniformly sampling on triangular faces, and poses of Gaussians are determined by face vertices. Inspired by GaMeS [39], we assign the rotation matrix R_v and scaling S_v of Gaussians based on vertices' positions. For a given triangular face V and its vertices $v_1, v_2, v_3 \in \mathbb{R}^3$, we define orthonormal vectors $r_1, r_2, r_3 \in \mathbb{R}^3$ to construct the rotation matrix $\mathrm{R}_v = [r_1, r_2, r_3]$. The vector r_1 is aligned with the normal vector of V to ensure Gaussians align with the triangular surface. The vector r_2 is defined as the vector from the center $m = \text{mean}(v_1, v_2, v_3)$ of the triangle to the first vertex v_1:

$$r_2 = \frac{v_1 - m}{||v_1 - m||}. \tag{2}$$

The last rotation vector r_3 is obtained by orthonormalizing the vector from the center to the second vertex concerning the existing r_1 and r_2 :

$$r_3 = \frac{ort(v_2 - m; r_1, r_2)}{||ort(v_2 - m; r_1, r_2||}, \tag{3}$$

where ort represents the orthonormalization in Gram-Schmidt [4]. For the scaling of 2D Gaussians, we use:

$$\mathrm{S}_v = \text{diag}(s_v^2, s_v^3), \tag{4}$$

where $s_v^2 = c||m - v_1||$, $s_v^3 = c < v_2, r_3 >$, and c is a size control hyperparameter. We place a fixed number of Gaussians on each triangular face. These designs eliminate the need to learn the geometry of Gaussians, focusing solely on their texture, thereby enhancing the efficiency of the representation.

Opacity Parameters. We define the total number of hybrid blocks as M. However, in practice, a typical scene does not contain exactly M blocks. Therefore, only the meaningful blocks are retained. To achieve this, we introduce a learnable parameter τ_i to represent each block's opacity. During the optimization process, only blocks with τ_i greater than a certain threshold are retained. Note that Gaussians on the same block share the same τ for opacity in rasterization.

Texture Parameters. The texture is modeled using 2D Gaussians positioned on the surface of the superquadrics. Spherical harmonics of each Gaussian control the texture and are optimized for rendering view-dependent images [18].

3.2. Optimizing the Hybrid Representation

This section describes the optimization of the hybrid representation. We found that minimizing the rendering loss across multi-view images alone led to instability in positioning hybrid blocks (primitives) accurately. Therefore, we introduce several regularizations and perform two optimization stages: block-level and point-level optimization.

3.2.1. Block-level Optimization

In addition to the image rendering loss, we employ regularizers consisting of coverage, overlap, parsimony, and opacity entropy. The coverage loss encourages hybrid blocks to cover only meaningful regions; the overlap loss prevents blocks from overlapping; the parsimony loss regularizes the number of existing blocks; and the opacity entropy encourages block opacities close to binary.

Rendering Loss. Based on the rendering process of Gaussian spaltting [18], the rendering loss is calculated by associating L_1 with a D-SSIM term[18] :

$$\mathcal{L}_{\text{ren}} = (1 - \lambda)\, L_1 + \lambda L_{\text{D-SSIM}}. \tag{5}$$

Coverage Loss. This loss ensures that the block set $\{\mathcal{B}_1 \dots \mathcal{B}_M\}$ covers the object while preventing it from extending beyond the object's boundaries. To determine the 3D occupancy field based on the blocks, we first define the approximate signed distance of a 3D point x to the i-th block, $D_i(x) = 1 - \Psi_i(x)$. Here, Ψ_i denotes the superquadric inside-outside function [2] associated with the block i. Consequently, $D_i(x) \geq 0$ if the point x lies inside the i-th block, and $D_i(x) < 0$ if x is outside the block. Inspired by NeRF [25], we sample a ray set $\mathcal{R}$ using ray-casting based on camera poses. Given the object mask, we associate each ray $r \in \mathcal{R}$ with a binary label: $l_r = 1$ if the ray r is inside mask, otherwise $l_r = 0$. The coverage loss is defined as:

$$\mathcal{L}_{\text{cov}}(\mathcal{R}) = \sum_{r \in \mathcal{R}} l_r L_{\text{cross}}(r) + (1 - l_r) L_{\text{non-cross}}(r). \tag{6}$$

Here, L_{cross} encourages rays to intersect with blocks, while $L_{\text{non-cross}}$ discourages rays from intersecting with blocks. They are defined as:

$$L_{\text{cross}}(r) = \text{ReLU}\Big(\min_{i \in \mathcal{M}} \min_{x_j^r \in \mathcal{X}_r} D_j(x_j^r)\Big), \tag{7}$$

$$L_{\text{non-cross}}(r) = \text{ReLU}\Big(\max_{i \in \mathcal{M}} \max_{x_j^r \in \mathcal{X}_r} -D_i(x_j^r)\Big), \tag{8}$$

where x_j^r means the j-th sampled points along the ray r and $\mathcal{M} = \{1, \dots M\}$. Intuitively, this means that there is at least one in sampled points $\mathcal{X}_r$ along the ray r inside the mask that lies within a certain block, while all points along the ray outside the mask should not lie within any block.

Overlap Loss. We add a regularization term to encourage individual blocks to remain non-overlapping. Given the difficulty of directly calculating block overlap, we use a Monte Carlo method similar to [27]. Practically, we sample multiple 3D points in space and penalize each point that lies inside more than k blocks. Based on the definition of the superquadric inside-outside function, we devise a soft occupancy function:

$$\mathcal{O}_i^x = \tau_i \,\text{sigmoid}(\frac{1 - \Psi_i(x)}{\gamma}), \tag{9}$$

where γ is a temperature parameter. Therefore, given a set of N sampled 3D points Ω, the overlap loss is expressed as:

$$\mathcal{L}_{\text{over}} = \frac{1}{N} \sum_{x \in \Omega} \text{ReLU} \left(\sum_{i \in \mathcal{M}} \mathcal{O}_i^x - k \right). \quad (10)$$

Parsimony Loss. To promote the use of the minimal number of blocks and achieve parsimony in decomposition, we add a loss term that regularizes the block opacity (τ). This loss is defined as:

$$\mathcal{L}_{\text{par}} = \frac{1}{M} \sum_{i \in \mathcal{M}} \sqrt{\tau_i}. \quad (11)$$

Opacity Entropy Loss. Naturally, during optimization, the opacity of the block inside the object region tends to approach 1, while the opacity of the block outside the object region tends to approach 0. To facilitate this, we associate the opacities of the blocks with the labeled rays. Specifically, we use a cross-entropy loss L_{ce}, between the opacity and mask labels as follows:

$$\mathcal{L}_{\text{opa}}(\mathcal{R}) = \frac{1}{|\mathcal{R}|} \sum_{r \in \mathcal{R}} L_{ce} \left(\max_{i \in \mathcal{M}} \tau_i(x^r), l_r \right). \quad (12)$$

Here, only points x^r inside the blocks are sampled, *e.g.*, $\{x^r \in \mathcal{X}_r \mid D_i(x^r) \leq 0\}$.

The total loss is the weighted summation of the loss terms described above:

$$\mathcal{L} = \mathcal{L}_{\text{ren}} + \lambda_{\text{cov}} \mathcal{L}_{\text{cov}} + \lambda_{\text{over}} \mathcal{L}_{\text{over}} + \lambda_{\text{par}} \mathcal{L}_{\text{par}} + \lambda_{\text{opa}} \mathcal{L}_{\text{opa}}. \quad (13)$$

Adaptive Number of Blocks. Given that the number of parts varies across scenes, we allow the number of blocks to adjust during optimization adaptively. When the opacity of an existing block falls below a threshold t, this block is immediately removed. Additionally, we explore a block-adding mechanism using point clouds that are randomly generated within the scene area. Specifically, we use DBSCAN [34] to cluster initial point clouds (*e.g.*, accessible by-products of COLMAP [33]) that are not covered by any blocks. A new block is then introduced at the center of each point cloud cluster. The other parameters of these new blocks are initialized randomly.

At last, block-level reconstruction gets a 3D scene composited by several superquadrics, as shown in Fig. 2.

3.2.2. Point-level Optimization

The primitive-based hybrid representation effectively decomposes the shape into parts but performs suboptimally for complex objects. To address this, we introduce a refinement stage for more precise geometry fitting. In this stage, we decouple the constraint between Gaussians and superquadrics, enabling the Gaussians to be freely optimized. Furthermore, to prevent Gaussian components from one block passing through another and disrupting the continuity and plausibility of the part decomposition, we impose a new constraint to minimize the negative signed distance of each Gaussian entering other blocks:

$$\mathcal{L}_{\text{enter}} = \frac{1}{N} \sum_{x \in \Omega} \sum_{m \in \mathcal{M} \setminus \{\delta\}} \text{ReLU}(-D_m(x)), \quad (14)$$

where Ω is the sampled Gaussian set, and δ represents the identifier of the block to which the Gaussian x belongs. As seen in Fig. 2, the reconstruction becomes more accurate and aligns better with the target shape after this stage.

4. Experiments

We evaluate our approach on 3D reconstruction quality, view synthesis, shape parsimony, and reconstruction time, comparing it with previous state-of-the-art methods.

4.1. Datasets

We conduct comparative experiments on two public datasets: DTU [17] and ShapeNet [6]. To validate the effectiveness of our method in man-made objects, we construct a ShapeNet subset with four categories: *Chair*, *Table*, *Gun*, and *Airplane*. The DTU dataset comprises 15 commonly used scenes, and each category in the ShapeNet dataset contains 15 objects. Additionally, to demonstrate our method's potential with real-world data, more qualitative results are presented on BlenderMVS dataset [45] and self-captured scenes.

4.2. Implementation Details

We build upon the 2DGS [16] architecture and add a non-learnable part attribute to each Gaussian component to enforce the constraint in Eq. 14. In the ShapeNet benchmark, we observe a common degradation in mesh reconstruction as shown in Fig. 7. To address this, we propose Gaussian scale regularization, as validated in Sec. 4.4. The same hyperparameters are used for all experiments. We set the initial number of primitives M to 8. The temperature parameter γ in Eq. 9 is 0.005 and the overlapping number k in Eq. 10 is 1.95. We train the hybrid representation for 30k iterations, followed by refinement optimization for another 30k iterations. During block-level optimization, the block-adding operation is carried out at the 5k-th and 10k-th iterations. The loss weights λ_{cov}, λ_{over}, λ_{par}, and λ_{opa} are set to 10, 1, 0.01, and 0.01, respectively. For more details on the dataset, metrics, baselines, and method, please refer to the supplementary materials.

4.3. Evaluations

4.3.1. DTU and Shapenet Benchmark

Geometry Reconstruction. In Tab. 1 and Tab. 3, we compare our geometry reconstruction to SOTA shape decomposition methods on Chamfer distance and training time using DTU

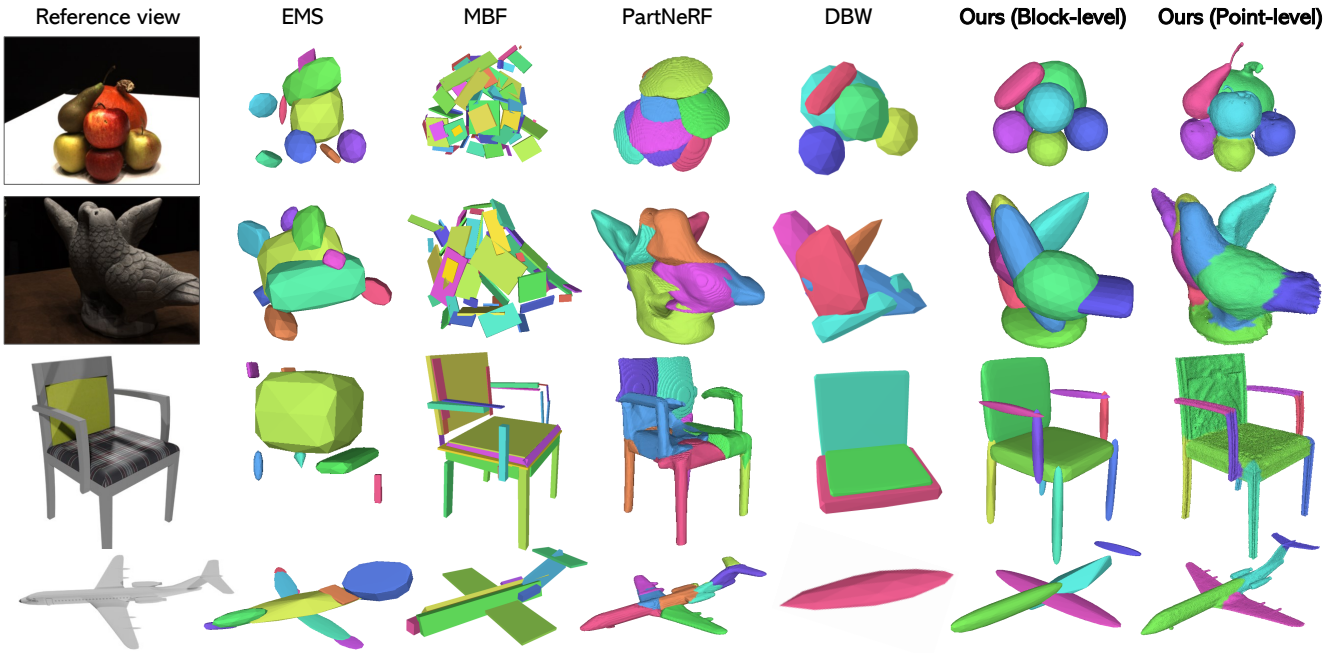

Figure 3. **Qualitative comparison on DTU [17] and ShapeNet [17] .** The first two rows are DTU examples, and the last two are ShapeNet examples, respectively. Our method is the only one that provides reasonable 3D part decomposition while capturing detailed geometry.

Method	Input	Renderable	Chamfer distance per scene															Mean CD	Mean #P
			S24	S37	S40	S55	S63	S65	S69	S83	S97	S105	S106	S110	S114	S118	S122		
EMS [22]	3D GT	✗	6.32	3.54	2.99	4.30	4.16	4.01	3.75	3.24	4.97	4.34	4.16	7.62	7.58	4.46	4.03	4.65	7.7
MBF [31]	3D GT	✗	3.12	2.66	3.84	2.54	1.59	2.11	2.19	2.01	2.32	2.45	2.17	2.12	3.83	2.02	2.55	2.50	34.1
EMS [22] + Neus [40]	Iamge	✗	5.99	5.56	4.43	4.32	5.42	6.14	3.75	3.96	4.63	4.34	5.88	5.11	4.29	4.83	3.53	4.97	8.87
MBF [31] + Neus [40]	Image	✗	2.69	3.37	3.22	2.69	3.63	2.60	2.59	3.13	2.85	2.51	2.45	3.72	2.24	2.49	2.52	2.85	46.7
PartNeRF [37]	Image	✓	9.38	10.46	9.08	8.63	6.04	7.25	7.22	9.15	8.72	10.01	6.72	9.85	7.85	8.68	9.21	8.54	8.0
DBW [27]	Image	✓	5.41	8.35	1.57	3.08	3.40	4.15	7.46	3.94	6.63	4.85	4.38	4.65	6.29	4.34	3.04	4.76	4.8
Ours (Block-level)	Image	✓	5.68	4.91	1.85	2.61	3.75	4.66	3.75	7.57	4.27	4.38	3.49	4.48	3.61	4.21	3.70	4.19	5.9
Ours (Point-level)	Image	✓	**0.95**	**1.38**	**0.55**	**0.71**	**1.02**	**1.39**	**1.16**	**1.33**	**1.49**	**0.80**	**0.95**	**1.31**	**0.69**	**1.20**	**0.82**	**1.05**	5.9

Table 1. **Quantitative comparison on DTU [17].** The Chamfer distance between the 3D reconstruction and the ground-truth is reported in 15 scenes. The best results are bolded, and the average numbers of primitives found (#P) that are greater than 10 are underlined.

Method	Part-aware	CD ↓	PSNR ↑	SSIM ↑	LIPPS ↓	Time ↓
Neuralangelo [21]	✗	0.61	33.84	-	-	> 10 h
2DGS [16]	✗	0.81	34.07	0.99	0.019	∼ 10 m
PartNeRF [37]	✓	9.59	17.97	0.77	0.246	∼ 8 h
DBW [27]	✓	4.73	16.44	0.75	0.201	∼ 2 h
Ours (Block-level)	✓	4.19	19.84	0.82	0.189	∼ 30 m
Ours (Point-level)	✓	**0.95**	**35.04**	**0.99**	**0.015**	∼ 40 m

Table 2. **Quantitative results on DTU** [17]. Our method outperforms all part-aware approaches in image synthesis quality, reconstruction accuracy, and efficiency. Neuralangelo's results are from the original paper, with all times measured on an RTX 3090 GPU.

Method	Input	Chamfer Distance ↓				Primitives (#P)				Mean	Mean
		Airplane	Table	Chair	Gun	Airplane	Table	Chair	Gun	CD	#P
EMS [22]	3D GT	3.40	6.92	19.0	2.02	9.4	7.88	10.3	8.4	7.84	9.0
MBF [31]	3D GT	2.83	2.18	1.59	2.32	10.85	13.9	13.4	14.3	2.21	13.1
PartNeRF [37]	Image	2.29	2.77	2.30	2.46	8.0	8.0	8.0	8.0	2.46	8.0
DBW [27]	Image	3.61	7.33	6.19	2.09	2.7	5.2	3.6	3.3	4.81	3.7
Ours (Block-level)	Image	2.47	2.15	2.32	1.78	3.9	6.6	7.6	5.0	2.18	5.8
Ours (Point-level)	Image	**1.29**	**1.72**	**0.94**	**1.07**	3.9	6.6	7.6	5.0	**1.25**	5.8

Table 3. **Quantitative comparison on ShapeNet [6].** We report Chamfer distance and the number of parts. The best results are bolded, and the second-best results are underlined.

and Shapenet dataset. Our method consistently outperforms in all scenes compared to prior works. As shown in Fig. 3, our approach consistently produces interpretable 3D decompositions with further refinement achieving more detailed geometry (the last two columns). MBF [31] achieves a low CD error but at the cost of using significantly more primitives, leading to over-decomposition and the inclusion of meaningless parts. Moreover, as shown in Tab. 2 and Tab. 4, our approach achieves competitive results with advanced Gaussian-based methods(*e.g.*, 2DGS [16]) and surface reconstruction approaches (*e.g.*, Neuralangelo [21]), which are limited to producing unstructured meshes. Notably, our

Method	Part-aware	Chamfer Distance ↓				PSNR ↑				SSIM ↑				LIPPS ↓			
		Airplane	Table	Chair	Gun	Airplane	Table	Chair	Gun	Airplane	Table	Chair	Gun	Airplane	Table	Chair	Gun
2DGS [16]	✗	1.47	2.37	0.50	1.03	40.89	39.80	39.05	41.74	0.994	0.990	0.990	0.994	0.009	0.027	0.017	0.009
PartNeRF [37]	✓	2.29	2.77	2.30	2.46	19.63	20.66	19.08	21.97	0.898	0.855	0.875	0.916	0.086	0.161	0.136	0.083
DBW [27]	✓	3.61	7.33	6.19	2.09	26.11	23.84	20.25	28.72	0.950	0.915	0.892	0.960	0.074	0.136	0.132	0.042
Ours (Block-level)	✓	2.47	2.15	2.32	1.78	27.94	27.98	24.92	29.95	0.959	0.925	0.906	0.963	0.072	0.129	0.122	0.047
Ours (Point-level)	✓	**1.29**	**1.72**	**0.94**	**1.07**	**41.18**	**36.80**	**36.07**	**39.51**	**0.992**	**0.973**	**0.977**	**0.989**	**0.014**	**0.070**	**0.038**	**0.021**

Table 4. **Quantitative results on ShapeNet** [6]. We report the Chamfer distance and novel view synthesis results across four categories.

Figure 4. **Qualitative results on BlenderMVS [45] and self-capatured data.** We present RGB renderings and decomposed parts from novel views. The top examples are from the BlenderMVS dataset, and the last example is from our captured scenes.

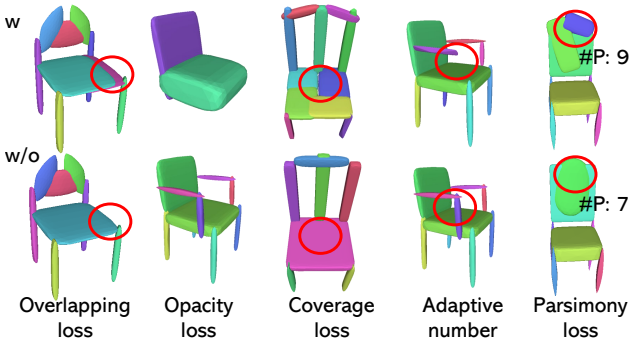

Figure 5. **Ablation studies on key strategies.** The block-level visual comparisons illustrate the impact of adopting our proposed strategy. The first row shows results without the strategy, and the second with the strategy implemented.

model demonstrates excellent efficiency, with a reconstruction speed approximately 10X faster than PartNeRF and over 3X faster than DBW.

Appearance Reconstruction. Beyond part decomposition, our method enables high-fidelity image synthesis, attributed to integrating Gaussian splatting within superquadric representations. EMS and MBF lack image rendering capabilities, while PartNeRF and DBW yield low-quality view synthesis. In contrast, our method achieves high-quality appearance rendering results, as demonstrated in Tab. 2 and Tab. 4.

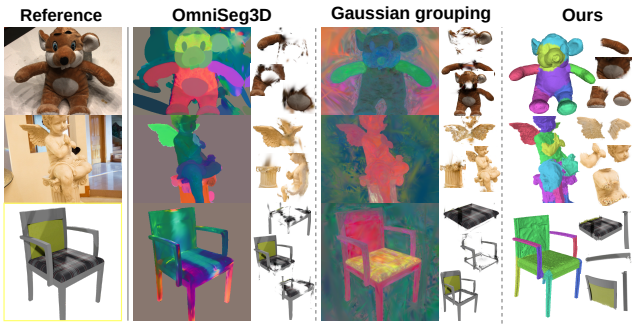

Figure 6. **Qualitative comparison with SAM-based methods**. Our method achieves finer-grained and more distinct part decomposition.

Method	Block-level				Point-level				
	CD ↓	PSNR ↑	SSIM ↑	LPIPS ↓	CD ↓	PSNR ↑	SSIM ↑	LPIPS ↓	#P
Complete model	2.32	24.92	0.906	0.122	0.94	36.07	0.977	0.038	6.6
w/o L_{over}	2.11	25.17	0.914	0.118	1.34	36.04	0.977	0.037	7.6
w/o L_{opa}	5.72	21.12	0.853	0.174	1.06	35.60	0.975	0.040	3.8
w/o L_{cov}	3.21	22.96	0.896	0.134	1.34	36.00	0.976	0.038	8.53
w/o Adaptive	3.16	22.74	0.880	0.141	1.05	35.74	0.974	0.040	6.7
w/o L_{par}	**1.91**	**25.48**	**0.918**	**0.115**	**0.93**	**36.18**	**0.977**	**0.037**	10.1

Table 5. **Ablation studies on the ShapeNet [6].** We report Chamfer Distance, rendering metrics, and the number of primitives (#P).

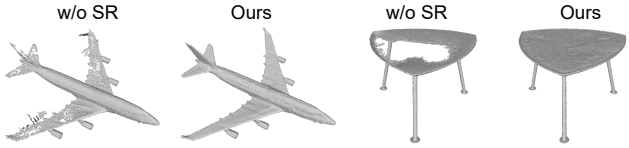

Figure 7. **Impact of Gaussian scale regularization (SR).** The degraded mesh produced by 2DGS [16] is effectively improved.

4.3.2. Real-life Data

To further demonstrate the applicability of our method for learning shape decomposition, we test our model on the real-life images from BlenderMVS dataset [45] and a self-captured dataset. As shown in Fig. 4, our approach can robustly produce both realistic appearances and meaningful 3D decompositions across a variety of data types. More results are provided in the supplementary material.

4.3.3. Compared to SAM-based Methods

We also conduct comparisons to SAM-based methods for this task, as shown in Fig. 6. Despite impressive advances in 3D segmentation and editing [5, 19, 46, 47] by distilling

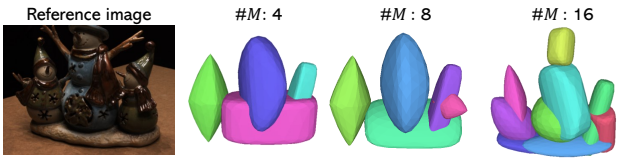

Figure 8. **Impact of the initial number of primitives (M).** Increasing M yields a finer-grained decomposition, while decreasing it produces a coarser decomposition.

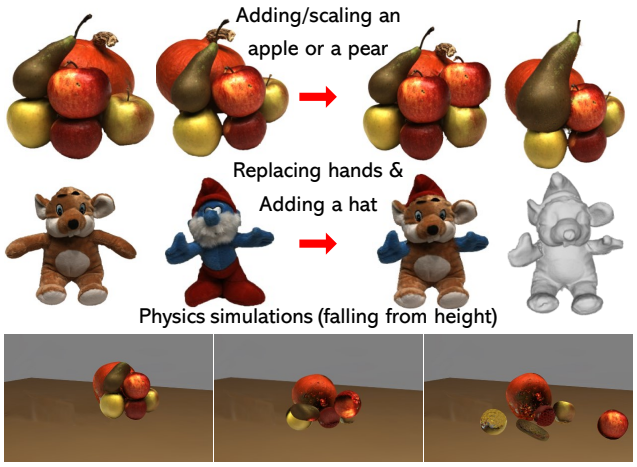

Figure 9. **Applications**. **Part-Aware Editing (top):** After optimization, we can easily edit the scene by adding, scaling, or moving specific parts. **3D Content Generation (middle):** By combining parts of different objects, we can create new 3D content. **Physics simulations (bottom)**: The representation enables us to perform physics-based simulations easily.

	Block-level				Point-level				
Method	CD ↓	PSNR ↑	SSIM ↑	LPIPS ↓	CD ↓	PSNR ↑	SSIM ↑	LPIPS ↓	#P
$\lambda_{\text{par}} = 0.1$	6.46	16.10	0.721	0.255	1.08	34.30	0.987	0.018	2.7
$\lambda_{\text{par}} = 0.01$ (*)	4.19	19.84	0.820	0.189	1.05	35.04	0.988	0.015	5.9
$\lambda_{\text{par}} = 0.001$	4.01	20.18	0.835	0.180	1.03	35.04	0.988	0.015	7.1
$M = 4$	4.97	19.06	0.794	0.213	1.06	34.93	0.987	0.016	5.0
$M = 8$ (*)	4.19	19.84	0.820	0.189	1.05	35.04	0.988	0.015	5.9
$M = 16$	3.99	20.87	0.83	0.176	1.07	35.05	0.988	0.015	8.3

Table 6. **Effect of parsimony weight (λ_{par}) and initial primitives count (M) on DTU [17].** We report Chamfer distance, rendering metrics, and primitives count (#P). * denotes the default setting.

2D information, achieving finer-grained semantic disentanglement remains challenging due to indistinct textures and severe cross-view 2D inconsistencies. Lifting 2D segmentation features to 3D segmentation will also lead to feature misalignment, leading to visual artifacts. In contrast, our method segments directly from 3D space, enabling more fine-grained and clearly defined component decomposition.

4.4. Ablations

In this section, we first analyze the design choices by isolating each strategy to assess its impact. We report the averaged quantitative performance on 15 instances of chair category in Tab. 5 and provide visual comparisons in Fig. 5. Removing overlapping loss enhances reconstruction quality but reduces semantic clarity. Omitting opacity loss drastically affects the number of primitives and doubles the CD, highlighting its role in controlling primitive presence and reconstruction accuracy. Coverage loss is crucial in reconstruction accuracy, ensuring primitives align correctly with the target. The adaptive primitive strategy fills in missing parts and improves the reconstruction metric. Without parsimony loss, CD and rendering metrics are optimal but result in redundancy and over-decomposition.

We also validate the effectiveness of Gaussian scale regularization in Fig. 7. 2DGS [16] tends to use large-scale Gaussians in texture-less areas and create holes in the constructed mesh by TSDF. Holes occur since large-scale Gaussians can't support consistent depth rendering from different views. Scale regularization effectively addresses this issue by suppressing large-scale Gaussians.

Lastly, in Tab. 6, we analyze the influence of two key hyperparameters on decomposition granularity: the parsimony loss weight λ_{par} and the initial primitive count M. Stronger parsimony regularization reduces the number of primitives, while weaker regularization increases it. As M rises, both reconstruction and view synthesis performance slightly improve. This demonstrates that adjusting M and λ_{par} enables our method to effectively control the granularity of object or scene decomposition. Fig. 8 visually illustrates this impact.

4.5. Applications

Fig. 9 illustrates three applications of our method that original 3DGS and NeRF-based approaches do not support. Firstly, after optimization, we obtain the part decomposition, facilitating easy editing of specific object or scene components, e.g., adding, moving, removing, or scaling. Secondly, by combining parts of different objects, our method enables the creation of new high-quality 3D content. Additionally, our method enables easy manipulation of objects within a scene, supporting physics-based simulations.

5. Conclusion

We introduce a hybrid representation of superquadrics and 2D Gaussians, to learn 3D scenes in a part-aware representation. Compared to prior works, the proposed method also keeps geometry details instead of shape abstractions, supporting high-level image rendering quality. The method gets state-of-the-art performance in comprehensive evaluations. One limitation is that the method takes background-free scenes as inputs, from segmentation tools such as SAM, as we care about the structure of the centered scene the most. In the future, we aim to explore how to model backgrounds and extend the work to address entire complex scenes.

References

[1] Stephan Alaniz, Massimiliano Mancini, and Zeynep Akata. Iterative superquadric recomposition of 3d objects from multiple views. In *Proceedings of the IEEE/CVF International Conference on Computer Vision (ICCV)*, pages 18013–18023, 2023. 2

[2] Alan H. Barr. Superquadrics and Angle-Preserving Transformations. *IEEE Computer Graphics and Applications*, 1981. 1, 3, 4

[3] Thomas Binford. Visual Perception by Computer. In *IEEE Conference on Systems and Control*, 1971. 2

[4] Åke Björck. Numerics of gram-schmidt orthogonalization. *Linear Algebra and Its Applications*, 197:297–316, 1994. 4

[5] Jiazhong Cen, Jiemin Fang, Chen Yang, Lingxi Xie, Xiaopeng Zhang, Wei Shen, and Qi Tian. Segment any 3d gaussians. *arXiv preprint arXiv:2312.00860*, 2023. 7

[6] Angel X. Chang, Thomas Funkhouser, Leonidas Guibas, Pat Hanrahan, Qixing Huang, Zimo Li, Silvio Savarese, Manolis Savva, Shuran Song, Hao Su, Jianxiong Xiao, Li Yi, and Fisher Yu. ShapeNet: An Information-Rich 3D Model Repository. *arXiv:1512.03012 [cs.CV]*, 2015. 5, 6, 7

[7] Hanlin Chen, Chen Li, and Gim Hee Lee. Neusg: Neural implicit surface reconstruction with 3d gaussian splatting guidance. *arXiv preprint arXiv:2312.00846*, 2023. 2

[8] Zhiqin Chen, Andrea Tagliasacchi, and Hao Zhang. Bsp-net: Generating compact meshes via binary space partitioning. In *2020 IEEE/CVF Conference on Computer Vision and Pattern Recognition (CVPR)*, 2020. 2

[9] Zhiqin Chen, Qimin Chen, Hang Zhou, and Hao Zhang. Dae-net: Deforming auto-encoder for fine-grained shape co-segmentation. *arXiv preprint arXiv:2311.13125*, 2023. 2

[10] Boyang Deng, Kyle Genova, Soroosh Yazdani, Sofien Bouaziz, Geoffrey Hinton, and Andrea Tagliasacchi. Cvxnet: Learnable convex decomposition. In *2020 IEEE/CVF Conference on Computer Vision and Pattern Recognition (CVPR)*, 2020. 2

[11] Ben Fei, Jingyi Xu, Rui Zhang, Qingyuan Zhou, Weidong Yang, and Ying He. 3d gaussian splatting as new era: A survey. *IEEE Transactions on Visualization and Computer Graphics*, pages 1–20, 2024. 2

[12] Martin A. Fischler and Robert C. Bolles. Random Sample Consensus: A Paradigm for Model Fitting with Applications to Image Analysis and Automated Cartography. *Communications of the ACM*, 1981. 2

[13] Lin Gao, Jie Yang, Bo-Tao Zhang, Jia-Mu Sun, Yu-Jie Yuan, Hongbo Fu, and Yu-Kun Lai. Mesh-based gaussian splatting for real-time large-scale deformation. *arXiv preprint arXiv:2402.04796*, 2024. 1, 2

[14] Yanran Guan, Han Liu, Kun Liu, Kangxue Yin, Ruizhen Hu, Oliver van Kaick, Yan Zhang, Ersin Yumer, Nathan Carr, Radomir Mech, et al. Fame: 3d shape generation via functionality-aware model evolution. *IEEE Transactions on Visualization and Computer Graphics*, 28(4):1758–1772, 2020. 2

[15] Antoine Guédon and Vincent Lepetit. Sugar: Surface-aligned gaussian splatting for efficient 3d mesh reconstruction and high-quality mesh rendering. *arXiv preprint arXiv:2311.12775*, 2023. 1, 2, 3

[16] Binbin Huang, Zehao Yu, Anpei Chen, Andreas Geiger, and Shenghua Gao. 2d gaussian splatting for geometrically accurate radiance fields. *SIGGRAPH*, 2024. 1, 2, 5, 6, 7, 8

[17] Rasmus Jensen, Anders Dahl, George Vogiatzis, Engil Tola, and Henrik Aanaes. Large Scale Multi-view Stereopsis Evaluation. In *CVPR*, 2014. 5, 6, 8

[18] Bernhard Kerbl, Georgios Kopanas, Thomas Leimkühler, and George Drettakis. 3d gaussian splatting for real-time radiance field rendering. *ACM Transactions on Graphics*, 42(4):1–14, 2023. 2, 4

[19] Chung Min* Kim, Mingxuan* Wu, Justin* Kerr, Matthew Tancik, Ken Goldberg, and Angjoo Kanazawa. Garfield: Group anything with radiance fields. In *Conference on Computer Vision and Pattern Recognition (CVPR)*, 2024. 7

[20] Lingxiao Li, Minhyuk Sung, Anastasia Dubrovina, Li Yi, and Leonidas J Guibas. Supervised Fitting of Geometric Primitives to 3D Point Clouds. In *CVPR*, 2019. 1

[21] Zhaoshuo Li, Thomas Müller, Alex Evans, Russell H Taylor, Mathias Unberath, Ming-Yu Liu, and Chen-Hsuan Lin. Neuralangelo: High-fidelity neural surface reconstruction. In *Proceedings of the IEEE/CVF Conference on Computer Vision and Pattern Recognition*, pages 8456–8465, 2023. 6

[22] Weixiao Liu, Yuwei Wu, Sipu Ruan, and Gregory S Chirikjian. Robust and Accurate Superquadric Recovery: a Probabilistic Approach. In *CVPR*, 2022. 1, 2, 3, 6

[23] Romain Loiseau, Elliot Vincent, Mathieu Aubry, and Loic Landrieu. Learnable Earth Parser: Discovering 3D Prototypes in Aerial Scans. *arXiv:2304.09704 [cs.CV]*, 2023. 1

[24] Tao Lu, Mulin Yu, Linning Xu, Yuanbo Xiangli, Limin Wang, Dahua Lin, and Bo Dai. Scaffold-gs: Structured 3d gaussians for view-adaptive rendering. *arXiv preprint arXiv:2312.00109*, 2023. 2

[25] Ben Mildenhall, Pratul P. Srinivasan, Matthew Tancik, Jonathan T. Barron, Ravi Ramamoorthi, and Ren Ng. NeRF: Representing Scenes as Neural Radiance Fields for View Synthesis. In *ECCV*, 2020. 1, 4

[26] Niloy Mitra, Michael Wand, Hao (Richard) Zhang, Daniel Cohen-Or, Vladimir Kim, and Qi-Xing Huang. Structure-aware shape processing. In *SIGGRAPH Asia 2013 Courses*, 2013. 1

[27] Tom Monnier, Jake Austin, Angjoo Kanazawa, Alexei A. Efros, and Mathieu Aubry. Differentiable Blocks World: Qualitative 3D Decomposition by Rendering Primitives. In *NeurIPS*, 2023. 1, 2, 3, 4, 6, 7

[28] Chengjie Niu, Jun Li, and Kai Xu. Im2struct: Recovering 3d shape structure from a single rgb image. *Cornell University - arXiv,Cornell University - arXiv*, 2018. 1

[29] Despoina Paschalidou, Ali Osman Ulusoy, and Andreas Geiger. Superquadrics Revisited: Learning 3D Shape Parsing Beyond Cuboids. In *CVPR*, 2019. 2

[30] Despoina Paschalidou, Luc Van Gool, and Andreas Geiger. Learning Unsupervised Hierarchical Part Decomposition of 3D Objects from a Single RGB Image. In *CVPR*, 2020. 2

[31] Michaël Ramamonjisoa, Sinisa Stekovic, and Vincent Lepetit. MonteBoxFinder: Detecting and Filtering Primitives to Fit a Noisy Point Cloud. In *ECCV*, 2022. 2, 3, 6

[32] Lawrence G. Roberts. *Machine perception of three-dimensional solids*. PhD thesis, Massachusetts Institute of Technology, 1963. 2

[33] Johannes Lutz Schönberger and Jan-Michael Frahm. Structure-from-motion revisited. In *Conference on Computer Vision and Pattern Recognition (CVPR)*, 2016. 5

[34] Erich Schubert, Jörg Sander, Martin Ester, Hans Peter Kriegel, and Xiaowei Xu. Dbscan revisited, revisited: why and how you should (still) use dbscan. *ACM Transactions on Database Systems (TODS)*, 42(3):1–21, 2017. 5

[35] Chunyu Sun, Yuqi Yang, Haoxiang Guo, Pengshuai Wang, Xin Tong, Yang Liu, and Heung-Yeung Shum. Semi-supervised 3d shape segmentation with multilevel consistency and part substitution. *Computational Visual Media*, 2022. 2

[36] Matthew Tancik, Ethan Weber, Evonne Ng, Ruilong Li, Brent Yi, Justin Kerr, Terrance Wang, Alexander Kristoffersen, Jake Austin, Kamyar Salahi, Abhik Ahuja, David McAllister, and Angjoo Kanazawa. Nerfstudio: A Modular Framework for Neural Radiance Field Development. In *SIGGRAPH*, 2023. 1

[37] Konstantinos Tertikas, Despoina Paschalidou, Boxiao Pan, Jeong Joon Park, Mikaela Angelina Uy, Ioannis Emiris, Yannis Avrithis, and Leonidas Guibas. PartNeRF: Generating Part-Aware Editable 3D Shapes without 3D Supervision. In *CVPR*, 2023. 1, 2, 6, 7

[38] Shubham Tulsiani, Hao Su, Leonidas J. Guibas, Alexei A. Efros, and Jitendra Malik. Learning Shape Abstractions by Assembling Volumetric Primitives. In *CVPR*, 2017. 1, 2

[39] Joanna Waczyńska, Piotr Borycki, Sławomir Tadeja, Jacek Tabor, and Przemysław Spurek. Games: Mesh-based adapting and modification of gaussian splatting. *arXiv preprint arXiv:2402.01459*, 2024. 1, 2, 3, 4

[40] Peng Wang, Lingjie Liu, Yuan Liu, Christian Theobalt, Taku Komura, and Wenping Wang. NeuS: Learning Neural Implicit Surfaces by Volume Rendering for Multi-view Reconstruction. In *NeurIPS*, 2021. 6

[41] Ruiqi Wang, Akshay Gadi Patil, Fenggen Yu, and Hao Zhang. Active coarse-to-fine segmentation of moveable parts from real images. *arXiv e-prints*, pages arXiv–2303, 2023. 2

[42] Xiaogang Wang, Yuelang Xu, Kai Xu, Andrea Tagliasacchi, Bin Zhou, Ali Mahdavi-Amiri, and Hao Zhang. Pie-net: Parametric inference of point cloud edges. *Advances in neural information processing systems*, 33:20167–20178, 2020. 1

[43] Tong Wu, Lin Gao, Ling-Xiao Zhang, Yu-Kun Lai, and Hao Zhang. Star-tm: Structure aware reconstruction of textured mesh from single image. *IEEE Transactions on Pattern Analysis and Machine Intelligence*, pages 1–14, 2021. 2

[44] Yuwei Wu, Weixiao Liu, Sipu Ruan, and Gregory S. Chirikjian. Primitive-based Shape Abstraction via Nonparametric Bayesian Inference. In *ECCV*, 2022. 1, 2

[45] Yao Yao, Zixin Luo, Shiwei Li, Jingyang Zhang, Yufan Ren, Lei Zhou, Tian Fang, and Long Quan. BlendedMVS: A Large-scale Dataset for Generalized Multi-view Stereo Networks. In *CVPR*, 2020. 5, 7

[46] Mingqiao Ye, Martin Danelljan, Fisher Yu, and Lei Ke. Gaussian grouping: Segment and edit anything in 3d scenes. In *ECCV*, 2024. 7

[47] Haiyang Ying, Yixuan Yin, Jinzhi Zhang, Fan Wang, Tao Yu, Ruqi Huang, and Lu Fang. Omniseg3d: Omniversal 3d segmentation via hierarchical contrastive learning. *arXiv preprint arXiv:2311.11666*, 2023. 7

[48] Fenggen Yu, Kun Liu, Yan Zhang, Chenyang Zhu, and Kai Xu. Partnet: A recursive part decomposition network for fine-grained and hierarchical shape segmentation. In *Proceedings of the IEEE/CVF conference on computer vision and pattern recognition*, pages 9491–9500, 2019. 1, 3

[49] Fenggen Yu, Yimin Qian, Xu Zhang, Francisca Gil-Ureta, Brian Jackson, Eric Bennett, and Hao Zhang. Dpa-net: Structured 3d abstraction from sparse views via differentiable primitive assembly. *arXiv preprint arXiv:2404.00875*, 2024. 1, 2

[50] Yu-Jie Yuan, Yang-Tian Sun, Yu-Kun Lai, Yuewen Ma, Rongfei Jia, Leif Kobbelt, and Lin Gao. Interactive nerf geometry editing with shape priors. *IEEE Transactions on Pattern Analysis and Machine Intelligence*, 2023. 2

[51] Chenyang Zhu, Kai Xu, Siddhartha Chaudhuri, Li Yi, Leonidas J Guibas, and Hao Zhang. Adacoseg: Adaptive shape co-segmentation with group consistency loss. In *Proceedings of the IEEE/CVF Conference on Computer Vision and Pattern Recognition*, pages 8543–8552, 2020. 1